

# Flexible polarimeter architecture based on a birefringent grating

Asticio Vargas,<sup>1,2</sup> Fabián A. Torres-Ruiz,<sup>1,2</sup> Juan Campos,<sup>3</sup> Ramiro Donoso,<sup>1,2</sup> José Luis Martínez,<sup>4</sup> and Ignacio Moreno<sup>4,\*</sup>

<sup>1</sup>Departamento de Ciencias Físicas, Universidad de La Frontera, Temuco, Chile

<sup>2</sup>Center for Optics and Photonics, University of Concepción, Casilla 4016, Concepción, Chile

<sup>3</sup>Departamento de Física, Universidad Autónoma de Barcelona, Barcelona, Spain

<sup>4</sup>Departamento de Ciencia de Materiales, Óptica y Tecnología Electrónica, Universidad Miguel Hernández de Elche, 03202 Elche, Spain

\*Corresponding author: i.moreno@umh.es

Received 30 May 2014; accepted 14 July 2014;  
posted 24 July 2014 (Doc. ID 213091); published 21 August 2014

A polarimeter architecture is presented based on a birefringent grating displayed onto a parallel-aligned liquid crystal (LC) on silicon display (PAL-LCoS). The system is compact and flexible, since the size of the image can be adjusted by means of the period of the grating. The LCoS grating permits simultaneously measuring two orthogonal states of polarization (SOPs). By adding a wave plate, different couples of orthogonal SOPs can be detected. First, a basic proof of concept is presented using one quarter-wave and one half-wave plate with fixed retardances, which permit measuring the six SOPs classically used in polarimetry (linear states at 0°, 45°, 90°, and 135°, and R and L circular states). Next, the system is made fully programmable by incorporating a variable LC retarder (LCR). The LCR orientation and retardance values are optimized by means of the condition number indicator, in order to provide equivalent optimal accuracy. Experimental results of calibration images and test images are presented, showing the potentials of this architecture. © 2014 Optical Society of America

OCIS codes: (260.5430) Polarization; (260.1440) Birefringence; (230.3720) Liquid-crystal devices; (110.5405) Polarimetric imaging; (050.1950) Diffraction gratings.

<http://dx.doi.org/10.1364/AO.53.005585>

## 1. Introduction

Polarimetry is a fundamental tool in current optical technology [1]. Whereas beam polarimetry permits the determination of the state of polarization (SOP) of a light beam, image polarimetry is employed when SOP measurements are required all over an image. In both cases, Stokes polarimetry is achieved by obtaining a set of irradiance measurements corresponding to projections of the input SOP onto different states defined by the polarization state detector (PSD). Mueller polarimetry refers to techniques where not only light is analyzed, but also a sample that modifies the SOP. In this case, different SOPs

are used to illuminate the sample, and the emerging SOP must be determined in each case. Multiple polarimetric techniques have been proposed, with many different features [2].

On the other hand, liquid-crystal (LC) modulators are devices based on a mature optoelectronic technology, widely available and very useful for real-time control of polarized light [3]. Thus, LC technology is becoming extensively used to substitute polarizing elements that require mechanical control. This helps to avoid moving elements in optical systems, thereby alleviating alignment procedures and thus producing automatic polarimeters [4]. Single-cell LC modulators are being used commonly in polarimetric systems [5–10]. Additionally, LC spatial light modulators (SLMs) are pixelated displays with enough spatial resolution to reproduce diffractive optical elements and com-

puter-generated holograms. In particular, since LC-SLMs act as pixelated and programmable birefringent elements, they can be used for the implementation of the so-called polarization diffraction gratings [11]. These are diffraction gratings based on spatially periodic SOP modification, and produce diffraction orders with specific and different SOP content, therefore having been proposed for polarimetric measurements [12].

In this paper, a fully programmable polarimeter optical system is presented that combines these two features of LC technology. First, one particular type of polarization grating, a birefringent blaze grating, is displayed onto a parallel aligned (PAL) LC on silicon (LCoS)-SLM, to act as a programmable polarizing beam splitter (PBS). Such a type of polarization grating is presented in Ref. [13] and, in combination with external wave plates (WPs), was proven to be a potential tool for polarimetric analysis. Such an LCoS-based PBS is employed here to split the incoming beam into two beams, which then project two orthogonal SOPs. Second, an LC retarder (LCR), i.e., a linear retarder with variable retardance controlled via an applied voltage, is used here as the external WP to modify the SOP of the incoming light. This permits changing the two orthogonal SOPs that are projected by the LCoS-PBS.

Three main novel features are presented in this work. First, the original birefringent blaze grating introduced in Ref. [13] is now adapted to a reflective architecture required by the use of an LCoS-SLM (the LC display employed in [13] was a transmissive PAL display). Therefore, the system can be compacted, although there are fewer degrees of freedom since the same external WP placed in front of the SLM is also acting on the reflected beam. Second, the use of an LCR as the external WP permits creating a fully programmable system, controlled from a computer, thus avoiding moving any element. Finally, we apply the condition number (CN) indicator [9] to determine the orientation and retardances of the LCR, which provide optimal accuracy of the polarimeter system, and we demonstrate that the LCR-based system provides polarimetric accuracy equivalent to that with the original system.

The outline of this paper is as follows: in Section 2, the birefringent polarization grating and its polarization splitting properties in a reflecting architecture are introduced, and a proof of concept is presented for its actuation as a beam polarimeter. Then, in Section 3, this basic system is made fully automatic by replacing the standard fixed WPs by a tunable LCR. The system is optimized to match the minimum CN in order to achieve the best accuracy. Section 4 presents experimental results as an imaging polarimeter. Finally, Section 5 presents the conclusions of this work.

## 2. Blazed Birefringent Grating

The blazed birefringent grating is a linear WP for which the ordinary phase shift is constant, but the

extraordinary phase shift grows linearly following the blazed grating phase profile. This type of polarization grating can be generated on a PAL LC-SLM by simply addressing the display with a saw-tooth gray level image [13]. Then, it acts as a PBS: whereas the linear polarization component parallel to the ordinary axis remains unaffected, the linear polarization component parallel to the extraordinary axis becomes diffracted to the first diffraction order with 100% efficiency. Note that it is possible to control the angle of deflection by simply changing the period of the diffraction grating.

Figure 1 shows the basic scheme of the polarimeter unit. A nonpolarizing BS is required to ensure normal incidence on the LCoS-SLM. A blazed diffraction grating is displayed on the SLM, thus acting as a PBS equivalent to that presented in Ref. [13]. However, the use of a reflective SLM allows producing a more compact polarimeter. Two beams are reflected back from the SLM, one with linear polarization parallel to the LC director and another with orthogonal linear polarization. These two reflected beams reach the BS. A converging lens is then placed on the path reflected from the BS. This lens focuses both beams in its back focal plane, generating two focalizations separated by a distance inversely proportional to the period of the grating displayed on the SLM. Note that this period can, therefore, be adjusted to the match size of the beam to be analyzed. Distances  $d_1$  and  $d_2$  (see Fig. 1) also are adjusted so there is an exact Fourier transform relation from the SLM plane to the CCD plane.

Note that the intensities of the two diffraction orders captured in the CCD are directly proportional to the square of the magnitude of the corresponding polarization components that are split by the grating displayed on the SLM. A WP can be inserted between the BS and the SLM, in order to change the polarization components of the incoming beam that are split, and in this way generate different PSDs required for polarimetric measurements. A full polarimetric

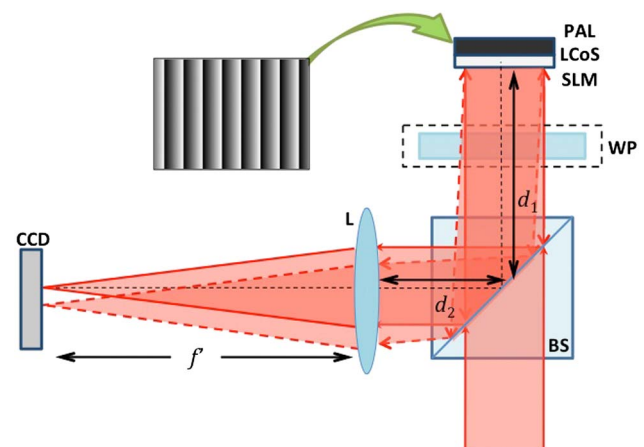


Fig. 1. Scheme of the optical architecture. The different polarizing elements that use each method are placed in position WP. BS is a nonpolarizing BS cube.

analysis requires measurements with different PSDs that are not located in a plane on the Poincaré sphere [9]. Since the proposed architecture provides two orthogonal PSD measurements at a time (because of the two-beam split at the SLM birefringent grating), it is necessary to select at least three different configurations, which provide six different PSD analyzers.

Initially we selected to sequentially add a quarter-wave plate (QWP) and a half-wave plate (HWP) to be able to measure the six classical SOPs employed in Mueller–Stokes polarimetry [14], i.e., linear polarization components at  $0^\circ$ ,  $45^\circ$ ,  $90^\circ$ , and  $-45^\circ$  (denoted as L0, L45, L90, and L-45, respectively), and circular R and L polarization components (denoted as RC and LC, respectively).

As the first proof of concept, we have developed a polarimeter that involves adding the QWP and HWP. In the absence of any WP, the LCoS-SLM grating splits the incoming beam into L0 and L90 components, which are, respectively, parallel and perpendicular to the orientation of the LC director of the LCoS-SLM. The insertion of the HWP oriented at  $22.5^\circ$  transforms the incoming L45 and L-45 polarization components onto L0 and L90, respectively. Therefore, the combined HWP-LCoS system effectively acts as a splitter of the L45 and L-45 linear components. Finally, the insertion of the QWP oriented at  $45^\circ$  transforms the QWP-LCoS system into an RC and LC polarization splitter. Therefore, the above-mentioned six classical polarization components required to achieve a complete polarimetric measurement can be obtained. The drawback, however, is that the WPs must be physically inserted into the system.

Figure 2 shows the first set of experimental results. We used a PAL LCoS-SLM from Holoeye, model NIR II with  $1920 \times 1080$  pixels and a pixel size of  $8 \mu\text{m} \times 8 \mu\text{m}$ , with a fill factor of 87%. The LC director was found to be oriented at  $84^\circ$  with respect to the vertical laboratory direction (this angle is, therefore, selected as the L0 polarization component). The system is illuminated with a He–Ne laser, from JDS Uniphase, model 1144P, at wavelength  $\lambda = 632.8 \text{ nm}$ . We used two birefringent polymer WPs from Meadowlarks, an HWP (model NHM-200-632.8) and a QWP (model NQM-200-632.8).

The figure shows 3D plots of the intensity recorded in the CCD plane. In Figs. 2(a)–2(c), the incident beam is selected to be L0 polarized. Therefore, the input polarization coincides with the LC director and the birefringent grating completely deflects the light onto the first diffraction order [Fig. 2(a)]. On the contrary, when the system is configured as an L45–L-45 splitter [Fig. 2(b)] or as an RC-LC splitter [Fig. 2(c)], two equally intense peaks are obtained corresponding to the 0 and +1 diffraction orders. The intensities of these peaks are half the intensity of the peak in Fig. 2(a), showing that the incoming L0 state splits with equal magnitude between these pairs of components.

Similar results appear in Figs. 2(d)–2(f), where now the input beam is selected to be L circularly polarized. In this case, the RC-LC splitter only shows

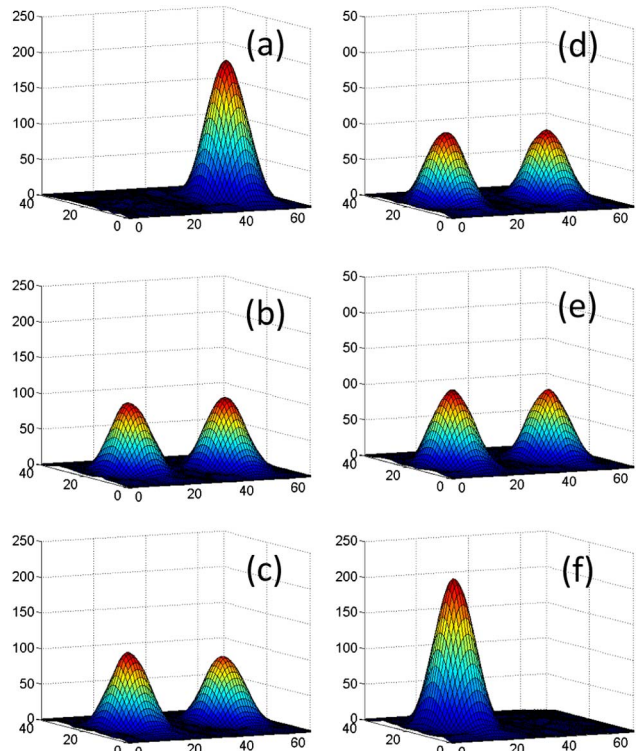


Fig. 2. Experimental results for beam polarimetry. In (a)–(c), the system is illuminated with L0 polarization, and in (d)–(f) with LC polarization. Panels (a) and (d) correspond to the L0–L90 splitter (no WP); (b) and (e) correspond to the L45–L-45 splitter (adding the HWP at  $22.5^\circ$ ); and (c) and (f) correspond to the RC-LC splitter (adding the QWP at  $45^\circ$ ).

one peak [Fig. 2(f)], which corresponds, in this case, to the zero diffracted order. On the contrary, when the system is configured to act as the L0–L90 and L45–L-45 splitters [Figs. 2(d) and 2(e), respectively], two equally intense peaks are produced.

### 3. Optimal Fully Programmable LCR-Based Polarimeter

These results show the usefulness of the proposed system to build a compact polarimeter. However, the requirement of physically changing the WPs limits its practical application and can be an important source of errors due to misalignments, additional reflections, etc. Therefore, we have considered a modification where an LCR is included in the system, to make it fully programmable. This device acts as a linear WP with a fixed orientation but variable retardance controlled with a computer. The LCR is a calibrated device from Meadowlark, model LRC-200 VIS [15]. In principle, two such LCR devices would be required to reproduce the polarimeter scheme in the previous section: one to act as the HWP and another to act as the QWP. However, as we show next, a single device is capable to produce an equivalent polarimeter, by properly selecting its orientation and retardance values.

CN has been revealed as an indicator that leads to polarimetry measurements with optimal accuracy

and reduced error propagation [9]. CN is defined in terms of the PSD analyzing the elements of the polarimeter. Let us consider a beam probe with a polarization state described by the Stokes parameters  $\mathbf{S} = (S_0, S_1, S_2, S_3)$ . This state is projected onto a PSD that can be configured into a number of different analyzers  $\mathbf{A}^i$  ( $i = 1, 2, \dots, n$ ). For each analyzer, the radiometric measurement  $I^i$  can be related to the Stokes parameters as  $I^i = \mathbf{A}^i \mathbf{S}$ , where  $\mathbf{A}^i = (A_0^i, A_1^i, A_2^i, A_3^i)$ . The information achieved with these different  $n$  analyzers can then be expressed in a matrix form as

$$\begin{pmatrix} I^1 \\ I^2 \\ \dots \\ I^n \end{pmatrix} = \begin{pmatrix} A_0^1 & A_1^1 & A_2^1 & A_3^1 \\ A_0^2 & A_1^2 & A_2^2 & A_3^2 \\ \dots & \dots & \dots & \dots \\ A_0^n & A_1^n & A_2^n & A_3^n \end{pmatrix} \begin{pmatrix} S_0 \\ S_1 \\ S_2 \\ S_3 \end{pmatrix}, \quad (1)$$

which can be written compactly as

$$\mathbf{I} = \mathbf{A} \mathbf{S}. \quad (2)$$

This relation can be inverted as

$$\mathbf{S} = \mathbf{A}^{-1} \mathbf{I} = \tilde{\mathbf{A}}^{-1} \mathbf{I}, \quad (3)$$

where  $\mathbf{A}^{-1}$  is the inverse,  $\tilde{\mathbf{A}}^{-1} = (\mathbf{A}^T \mathbf{A})^{-1} \mathbf{A}^T$  is the pseudo-inverse, and  $\mathbf{A}^T$  is the transposed of matrix  $\mathbf{A}$ .

At least four linearly independent analyzers are required to completely determine the input Stokes parameters. Because our system provides two analyzers in each measurement, at least three measurements are required and then six analyzers are being applied. By choosing the different analyzers' matrix  $\mathbf{A}$ , different polarimeters are built with different accuracy in the presence of measurement error. CN is the metric that permits comparing different polarimeters. This parameter is defined as [9]

$$\text{CN}(\mathbf{A}) = \frac{\sigma_{\max}}{\sigma_{\min}}, \quad (4)$$

where  $\sigma_{\max}$  and  $\sigma_{\min}$  are, respectively, the maximum and minimum singular values different from zero of matrix  $\mathbf{A}$ . Minimizing this parameter leads to the optimal system in terms of polarimeter measurements.

For instance, the polarimeter system described in Section 2 is composed of six different analyzers, which project onto SOPs L0, L90, L45, L-45, RC, and LC. Therefore, the analyzer matrix for this polarimeter is given by

$$\mathbf{A}_m = \begin{pmatrix} +1 & +1 & 0 & 0 \\ +1 & -1 & 0 & 0 \\ +1 & 0 & +1 & 0 \\ +1 & 0 & -1 & 0 \\ +1 & 0 & 0 & +1 \\ +1 & 0 & 0 & -1 \end{pmatrix}. \quad (5)$$

Here sub-index "m" refers to the fact that the WP elements must be inserted manually into this system.

The related condition number is  $\text{CN} = 1.7321$ , which is the lowest value that can be obtained [9].

The same procedure has been applied to the LCR-based system. Here, two parameters must be determined: LCR orientation, which is a fixed value, and LCR retardance, which is a tunable parameter. The minimum CN result is obtained with an orientation of  $27.4^\circ$  and retardances of  $0^\circ$ ,  $120^\circ$ , and  $240^\circ$ , leading again to  $\text{CN} = 1.7321$ , i.e., the same optimal value as in the case presented in Section 2. The corresponding matrix  $\mathbf{A}$  is given by

$$\mathbf{A}_{lcr} = \begin{pmatrix} +1 & +1 & 0 & 0 \\ +1 & -1 & 0 & 0 \\ +1 & 0 & +\sqrt{2}/2 & -\sqrt{2}/2 \\ +1 & 0 & -\sqrt{2}/2 & +\sqrt{2}/2 \\ +1 & 0 & +\sqrt{2}/2 & +\sqrt{2}/2 \\ +1 & 0 & -\sqrt{2}/2 & -\sqrt{2}/2 \end{pmatrix}. \quad (6)$$

Therefore, the fully programmable system incorporating the LCR can achieve a CN equivalent to that of the optimal system in Section 2. Thus, this LCR-based polarimeter provides polarimetric results with equivalent accuracy. The reason is that the six analyzers selected for both polarimeters provide, except a rotation, an equivalent geometrical figure. This is visualized in Fig. 3, where the analyzers for both polarimeters are visualized in the Poincaré sphere. In both cases, these SOPs define an octahedron, thus providing the same volume, which is directly related to the obtained equivalent CN value [9].

In the following section, we present the experimental results for both systems.

#### 4. Experimental Imaging Polarimeter

For this experiment, the system is now modified to become an imaging polarimeter. This is achieved by simply moving the converging lens slightly, so that the CCD plane is conjugated to a transverse plane located before the BS in Fig. 1. A circular aperture is placed in this plane.

##### A. Calibration

When building an experimental polarimeter, different sources of error might affect the results, including the

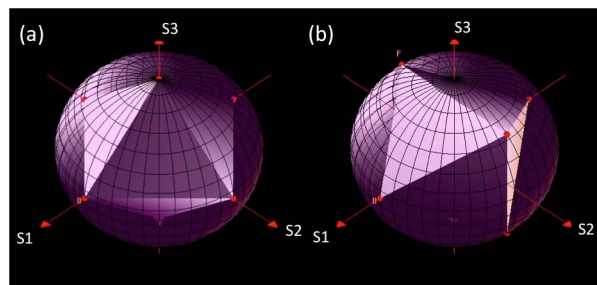


Fig. 3. Representation on the Poincaré sphere of the six analyzers for (a) the manual polarimeter and (b) the LCR-based programmable polarimeter. Both polarimeters produce, except a rotation, an equivalent geometrical octahedron, thus providing equivalent accuracy.

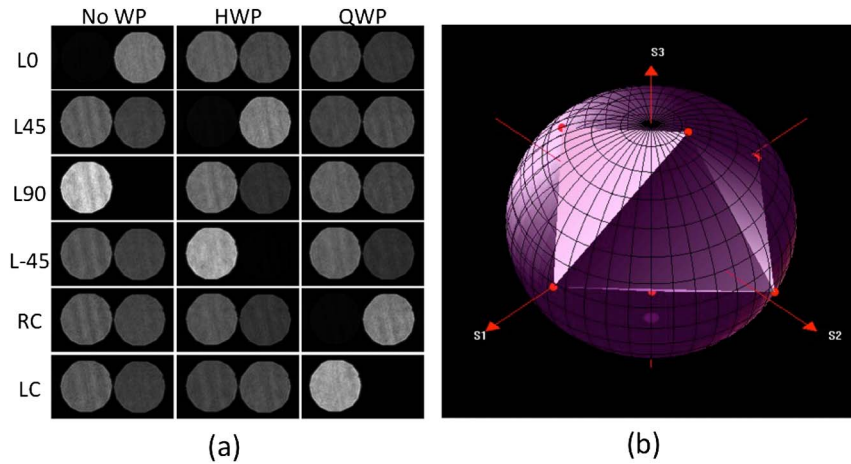


Fig. 4. (a) Experimental captures for the calibration of the imaging manual polarimeter. (b) Representation on the Poincaré sphere of the experimental analyzers.

nonideal behavior of some optical elements, possible misalignments, etc. In order to take them into account, the experimental matrix  $\mathbf{A}$  is calibrated by launching several well-defined input SOPs to the polarimeter and measuring the corresponding irradiances. We used the six standard SOPs

$$\mathbf{L0} = \begin{pmatrix} +1 \\ +1 \\ 0 \\ 0 \end{pmatrix}, \quad \mathbf{L90} = \begin{pmatrix} +1 \\ -1 \\ 0 \\ 0 \end{pmatrix}, \quad \mathbf{L45} = \begin{pmatrix} +1 \\ 0 \\ +1 \\ 0 \end{pmatrix},$$

$$\mathbf{L-45} = \begin{pmatrix} +1 \\ 0 \\ -1 \\ 0 \end{pmatrix}, \quad \mathbf{RC} = \begin{pmatrix} +1 \\ 0 \\ 0 \\ +1 \end{pmatrix}, \quad \mathbf{LC} = \begin{pmatrix} +1 \\ 0 \\ 0 \\ -1 \end{pmatrix}. \quad (7)$$

These input SOPs are analyzed with the different analyzers  $A^i$  and the corresponding irradiances are measured. Then the analyzer matrix elements are given by

$$A_0^i = \frac{1}{2}(I_{L0}^i + I_{L90}^i), \quad A_1^i = \frac{1}{2}(I_{L0}^i - I_{L90}^i),$$

$$A_2^i = \frac{1}{2}(I_{L45}^i - I_{L-45}^i), \quad A_3^i = \frac{1}{2}(I_{RC}^i - I_{LC}^i). \quad (8)$$

Figures 4 and 5 show the experimental results for this procedure, for the two polarimetric systems considered here: the initial system in Section 2 and the fully programmable system in Section 3. In this calibration process, the input beam is selected uniformly polarized in the six SOPs defined in Eq. (7). Each figure presents a set of 18 images. For each of the six input SOPs in Eq. (7), three images are captured, corresponding to the three polarimeter configurations. Each CCD capture contains two images of the circular aperture, which is selected as the input scene. These two images correspond to the two beams generated by the LCoS-SLM. The irradiance of these images depends on the input SOP illuminating the aperture and the selected configuration of the polarimeter. Therefore, the two images in the final plane should be a uniform disk. However, some interference

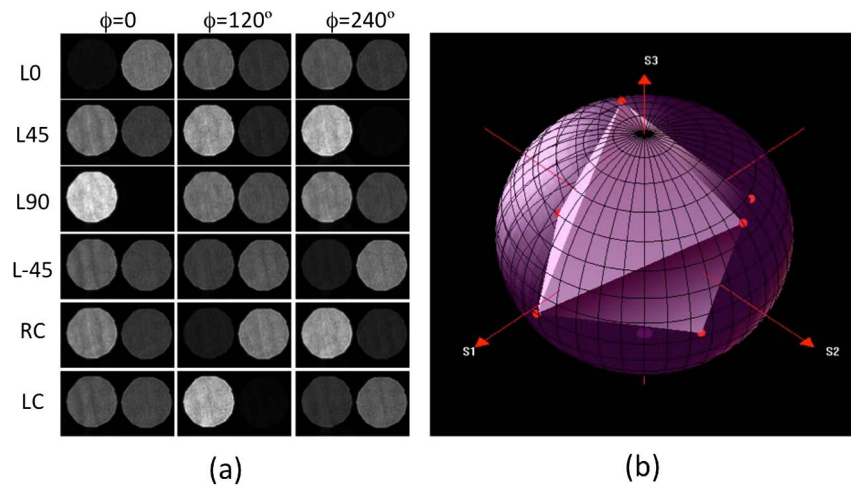


Fig. 5. (a) Experimental captures for the calibration of the imaging LCR-based programmable polarimeter. (b) Representation on the Poincaré sphere of the experimental analyzers.

effects can be present in the images, originating from reflections at the LCoS-SLM, as well as some diffraction at the circular aperture.

In all cases, the two images of the circular aperture in each of the CCD camera captures are extracted and aligned digitally, in order to make the required operations. With the data in Figs. 4 and 5, we have calculated the matrices corresponding to the analyzers' matrix  $\mathbf{A}$  for both experimental polarimeters. The values are averaged over the complete circular aperture in order to compute these experimental analyzers, and the resulting SOPs are represented in the Poincaré sphere in Figs. 4(b) and 5(b).

For the manual polarimeter system, the resulting matrix  $\mathbf{A}$  is given by

$$\mathbf{A}_m^{\text{exp}} = \begin{pmatrix} +1 & +0.98 & +0.04 & +0.05 \\ +1 & -0.97 & +0.05 & +0.01 \\ +1 & -0.22 & +0.97 & -0.19 \\ +1 & -0.07 & -0.92 & +0.26 \\ +1 & -0.13 & +0.22 & +0.98 \\ +1 & -0.16 & -0.16 & -0.94 \end{pmatrix}, \quad (9a)$$

with an experimental condition number  $\text{CN}_m^{\text{exp}} = 2.04$ . These represent the mean values averaged over a large number of pixels. The corresponding variance value for each matrix element was calculated, the results being

$$\mathbf{V}_m^{\text{exp}} = \begin{pmatrix} 0 & 0.02 & 0.05 & 0.06 \\ 0 & 0.01 & 0.06 & 0.07 \\ 0 & 0.05 & 0.02 & 0.06 \\ 0 & 0.06 & 0.02 & 0.05 \\ 0 & 0.05 & 0.06 & 0.02 \\ 0 & 0.05 & 0.05 & 0.02 \end{pmatrix}. \quad (9b)$$

Note that all variance values are below 0.07.

For the fully programmable LCR-based system, the measured experimental analyzer matrix  $\mathbf{A}$  is given by

$$\mathbf{A}_{lcr}^{\text{exp}} = \begin{pmatrix} +1 & +0.97 & -0.04 & -0.13 \\ +1 & -0.89 & +0.11 & -0.20 \\ +1 & -0.10 & +0.44 & -0.74 \\ +1 & -0.20 & -0.41 & +0.89 \\ +1 & -0.18 & +0.75 & +0.52 \\ +1 & -0.09 & -0.89 & -0.48 \end{pmatrix}, \quad (10a)$$

with an experimental condition number  $\text{CN}_{lcr}^{\text{exp}} = 2.49$ . The corresponding variance values of the matrix elements are

$$\mathbf{V}_{lcr}^{\text{exp}} = \begin{pmatrix} 0 & 0.01 & 0.05 & 0.06 \\ 0 & 0.02 & 0.07 & 0.08 \\ 0 & 0.06 & 0.05 & 0.03 \\ 0 & 0.06 & 0.07 & 0.02 \\ 0 & 0.05 & 0.03 & 0.05 \\ 0 & 0.06 & 0.02 & 0.06 \end{pmatrix}. \quad (10b)$$

Therefore, we can see that both experimental systems provide slightly higher CN values compared with the theoretical ones, and they both show similar values of the variance of the analyzer matrix elements. The LCR-based system provides a worse CN value than the system based on alternating WPs. We attribute this effect to the better WP quality of the polymer WPs in comparison with the LCR WP, which presents a small variation of the retardance over its aperture, as pointed out in [15].

## B. Comparison of Performance with a Predefined SOP

Once both experimental polarimeters have been calibrated, we have applied them to measure a beam with a uniform linear SOP oriented at  $30^\circ$ . The experimental measurements are provided in Figs. 6 and 7. In Fig. 6, the results are obtained with the first system, presented in Section 2. Figure 6(a) shows the three CCD captures corresponding to the three configurations of the polarimeter (without WP, with the

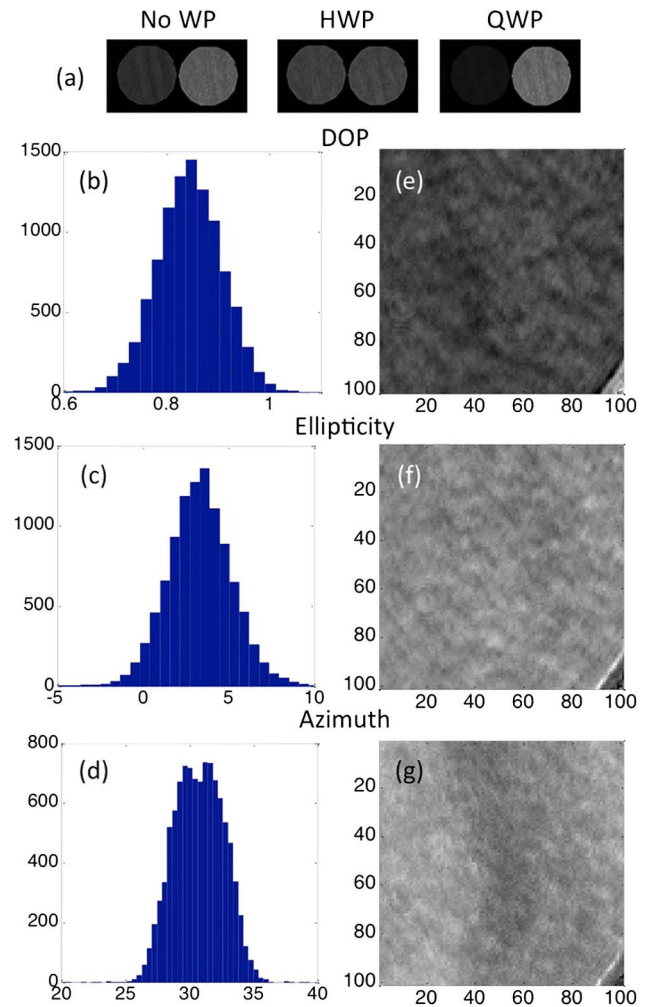


Fig. 6. Experimental results for the manual imaging polarimeter for a test beam with the L30 SOP: (a) three direct CCD captures. Histograms over the entire circular aperture of (b) DOP, (c) ellipticity, and (d) azimuth. Panels (e), (f), and (g) show, respectively, the corresponding DOP, ellipticity, and azimuth images for a fixed small portion of the circular aperture.

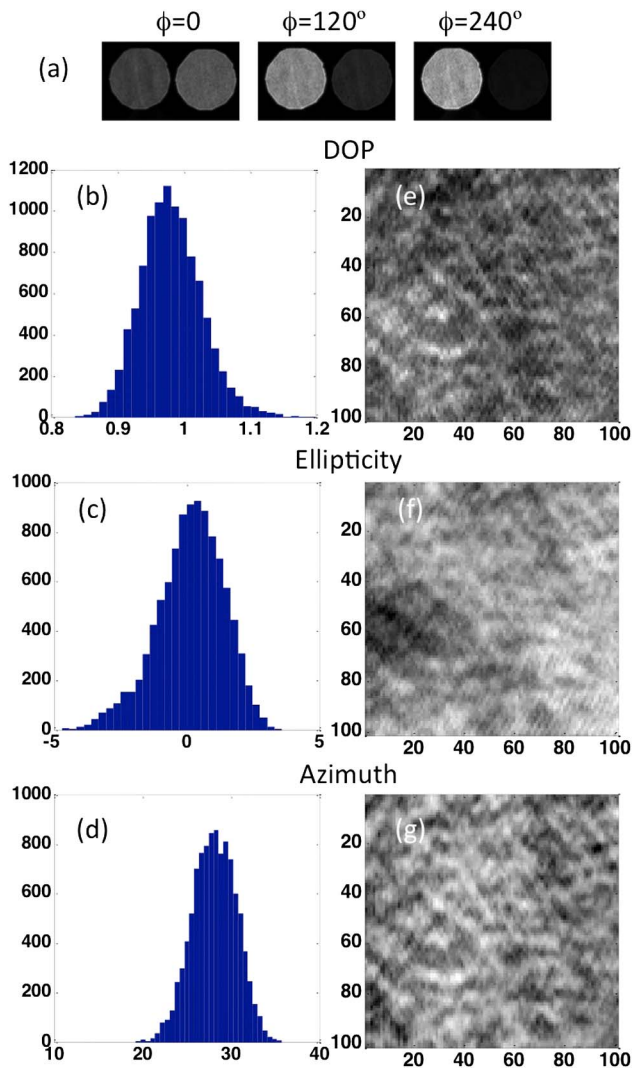


Fig. 7. Experimental results for the LCR-based programmable imaging polarimeter for a test beam with L30 SOP: (a) three direct CCD captures; histograms over the entire circular aperture of: (b) DOP, (c) ellipticity, and (d) azimuth. Panels (e), (f), and (g) show, respectively, the corresponding DOP, ellipticity, and azimuth images for a fixed small portion of the circular aperture.

HWP, and with the QWP), each showing the two images of the circular aperture. Again, because the system is acting as an imaging polarimeter, we can evaluate the polarimetric measurement over the entire circular aperture. Figures 6(b), 6(c), and 6(d) show, respectively, the histogram of the results obtained for the degree of polarization (DOP), ellipticity, and azimuth angles (expressed in degrees), calculated over all pixels of the complete image of the circular aperture. From these histograms, it can be seen that the polarimeter is providing a correct result, a linear polarization state oriented at  $30^\circ$ , with a small spatial variation. In order to see these variations clearly, a fixed small portion of the DOP, ellipticity, and azimuth images is presented in Figs. 6(e), 6(f), and 6(g), respectively, where the gray levels of the images present the values normalized to the corresponding minimum (zero gray level) and

Table 1. Comparison of the Expected and Experimental Measurements of the Two Polarimeter Systems Applied to Measure the SOP of a Laser Beam with Uniform Linear Polarization Oriented at  $30^\circ$  (L30)

	Theory	System I with Manual WPs	System II with Tunable LCR
CN	1.7321	2.04	2.49
$S_0$	1	0.99	1.01
$S_1$	0.5	+0.51	+0.54
$S_2$	$\sqrt{3}/2 = 0.8660$	+0.79	+0.82
$S_3$	0	-0.04	+0.02
DOP	1	0.95	0.97
Ellipticity	$0^\circ$	$-1.2^\circ$	$+0.6^\circ$
Azimuth	$30^\circ$	$28.5^\circ$	$28.2^\circ$

maximum (255 gray level) value over the circular aperture.

Figure 7 shows the equivalent results, but obtained with the LCR-based fully programmable polarimeter in Section 3. The results are similar to those presented in Fig. 6. The polarimetric images in Figs. 7(e)–7(g) show more variations than the equivalent Figs. 6(e)–6(g). We attribute this to the small spatial variations of LCR retardance described in [15].

Table 1 gives the mean values averaged over the full image for the measured Stokes parameters, DOP, and azimuth and ellipticity angles. We see that both polarimeters provide very similar results, and close to the theoretical ones, thus verifying that the programmable polarimeter is able to achieve equivalent accuracy.

## 5. Conclusions

In summary, we have developed a novel polarimetric architecture based on the use of a birefringent polarization grating displayed onto an LCoS-SLM. The optical system, therefore, is compact and also flexible. The grating period can be changed with a computer to match the size of the beam and the phase depth can also be adapted to match the operating wavelength. We have presented the first proof of concept acting as a beam polarimeter and a Fourier transform architecture, and using two external fixed-retardance WPs. Then we have compared the performance with a fully programmable polarimeter that incorporates one single LCR. We have optimized this system on the basis of the best CN indicator, in order to select the LCR orientation and retardance values, and we have demonstrated that it provides equivalent accuracy. Experimental results have been presented, where the system is adapted to act as an imaging polarimeter. Comparable results have been obtained with both polarimeter systems.

This work has been financed by grants Fondecyt Nos. 1110937 and 11110258 (Chile), the Center for Optics and Photonics (CEFOP) FB0824/2008, and the Ministerio de Economía y Competitividad (Spain) and Fondos FEDER through projects FIS2012-39158-C02-01 and 02.

## References

1. D. Goldstein, *Polarized Light* (Marcel Dekker, 2004).
2. R. A. Chipman, "Polarimetry," in *Handbook of Optics*, 2nd ed. (McGraw-Hill, 1995), pp. 22.1–22.37.
3. J. Beeckman, K. Neyts, and P. J. M. Vanbrabant, "Liquid-crystal photonic applications," *Opt. Eng.* **50**, 081202 (2011).
4. J. M. Bueno and S. Drobczynski, "Automatized imaging polarimetry with carrier frequency: influence of the initial phase and diattenuation," *Opt. Pura Apl.* **40**, 57–64 (2007).
5. J. M. Bueno, "Polarimetry using liquid-crystal variable retarders: theory and calibration," *J. Opt. A* **2**, 216–222 (2000).
6. S. L. Blakeney, S. E. Day, and J. N. Stewart, "Determination of unknown input polarisation using a twisted nematic liquid crystal display with fixed components," *Opt. Commun.* **214**, 1–8 (2002).
7. A. De Martino, Y. K. Kim, E. Garcia-Caurel, B. Laude, and B. Drévilon, "Optimized Mueller polarimeter with liquid crystal," *Opt. Lett.* **28**, 616–618 (2003).
8. S. Firdous and M. Ikram, "Stokes polarimetry for the characterization of bio-materials using liquid crystal variable retarders," *Proc. SPIE* **6632**, 66320F (2007).
9. A. Peinado, A. Lizana, J. Vidal, C. Iemmi, and J. Campos, "Optimization and performance criteria of a Stokes polarimeter based on two variable retarders," *Opt. Express* **18**, 9815–9830 (2010).
10. A. Peinado, A. Lizana, J. Vidal, C. Iemmi, and J. Campos, "Optimized Stokes polarimeters based on a single twisted nematic liquid-crystal device for the minimization of noise propagation," *Appl. Opt.* **50**, 5437–5445 (2011).
11. G. Cincotti, "Polarization gratings: design and applications," *IEEE J. Quantum Electron.* **39**, 1645–1652 (2003).
12. F. Gori, "Measuring Stokes parameters by means of a polarization grating," *Opt. Lett.* **24**, 584–586 (1999).
13. J. A. Davis, J. Adachi, C. R. Fernández-Pousa, and I. Moreno, "Polarization beam splitters using polarization diffraction gratings," *Opt. Lett.* **26**, 587–589 (2001).
14. A. Márquez, I. Moreno, C. Iemmi, A. Lizana, J. Campos, and M. J. Yzuel, "Mueller–Stokes characterization and optimization of a liquid crystal on silicon display showing depolarization," *Opt. Express* **16**, 1669–1685 (2008).
15. A. Vargas, R. Donoso, M. Ramírez, J. V. Carrión, M. M. Sánchez-López, and I. Moreno, "Liquid crystal retarder spectral retardance characterization based on a Cauchy dispersion relation and a voltage transfer function," *Opt. Rev.* **20**, 378–384 (2013).